ACS NANO

www.acsnano.org

ARTICLE

# Modulating the Energy Barrier via the Synergism of $Cu_3P$ and CoP to Accelerate Kinetics for Bolstering Oxygen Electrocatalysis in Zn-Air Batteries

Man Guo,[§] Lixia Wang,[§] Zhiyang Huang, Huatong Li, Tayirjan Taylor Isimjan, and Xiulin Yang*

Cite This: *ACS Nano* 2024, 18, 17901−17912

Read Online

ACCESS | Metrics & More | Article Recommendations | Supporting Information

**ABSTRACT:** **Modulating the energy barrier of reaction intermediates to surmount sluggish kinetics is an utterly intriguing strategy for amplifying the oxygen reduction reaction. Herein, a $Cu_3P$/CoP hybrid is incorporated on hollow porous N-doped carbon nanospheres via dopamine self-polymerization and high-temperature treatment. The resultant $Cu_3P$/CoP@NC showcases a favorable mass activity of 4.41 mA $mg^{-1}$ and a kinetic current density of 2.38 mA $cm^{-2}$. Strikingly, the catalyst endows the aqueous Zn-air battery (ZAB) with a large power density of 209.0 mW $cm^{-2}$, superb cyclability over 317 h, and promising application prospects in flexible ZAB. Theoretical simulations reveal that Cu functions as a modulator to modify the free energy of intermediates and adsorbs the $O_2$ on the Co sites, hence rushing the reaction kinetics. The open and hydrophilic hollow spherical mesoporous structure provides unimpeded channels for reactant diffusion and electrolyte penetration, whereas the exposed inner and outer surfaces can confer a plethora of accessible actives sites. This research establishes a feasible design concept to tune catalytic activity for non-noble metal materials by construction of a rational nanoframework.**

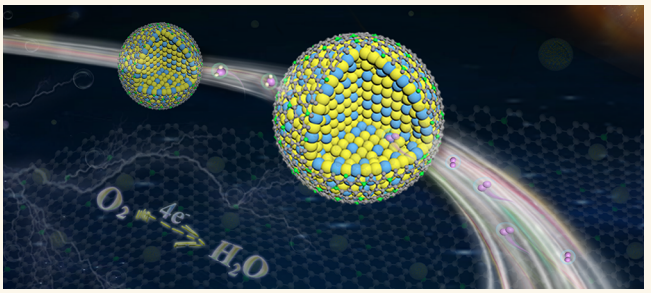


**KEYWORDS:** *energy barrier, $Cu_3P$/CoP, Zn-air battery, hollow spherical mesoporous structure, reaction kinetics*

## INTRODUCTION

The Zn-air battery (ZAB) with environmental benignity, inherent safety, and exceptional theoretical energy density (1086 Wh $kg^{-1}$) has been spotlighted as a burgeoning initiative to relieve energy shortages.[1,2] The energy efficiency and longevity of ZAB hinge predominantly on the superior oxygen reduction reaction (ORR) electrocatalysts.[3] Nonetheless, the ORR's sluggish kinetics rendered by multiple electron transfer process has sharply hampered the commercial viability of ZAB while spurring the exploitation for potent electrocatalysts.[4,5] Although noble-metal-based compounds (especially those with platinum) indicated superior ORR activity, the earth-finite availability, prohibitive prices, and susceptibility to deactivation remained obstacles to widespread applications.[6−8] In this regard, the exploration and development of competitive non-noble-metal catalysts as burgeoning and promising alternatives have become focal points.

Nowadays, the nonprecious metal materials, including sulfides,[9] phosphides,[10] and nitrides,[11,12] have garnered incremental attention because of cost-effectiveness and decent performance. Phosphorus (P) atoms will restrict the electron delocalization of metal elements due to slightly higher electronegativity, allowing P to capture protons and facilitate electron transfer in transition metal phosphides (TMPs).[13,14] However, the troubles of low conductivity and active site availability have led to less reports on invoked in ZAB. Alternatively, efficacious tactics for integrating TMPs with highly conductive supports, such as graphene,[15,16] carbon nanotubes,[17] and hollow porous carbon framework,[18] have been manifested to overcome the above obstacles. Specifically, active components could be loaded onto hollow porous supports to inhibit the agglomeration and deactivation of metal ions. Synchronously, the holistic optimization furnishes the

Received: April 4, 2024
Revised: May 29, 2024
Accepted: June 10, 2024
Published: June 24, 2024

Downloaded via GUANGXI NORMAL UNIV on July 10, 2024 at 02:01:08 (UTC).
See https://pubs.acs.org/sharingguidelines for options on how to legitimately share published articles.

ACS Publications

© 2024 American Chemical Society



https://doi.org/10.1021/acsnano.4c04479
*ACS Nano* 2024, 18, 17901−17912

catalyst with greater electrical conductivity and specific surface area.[19,20] The hollow porous framework augments intrinsic activity and minimizes the obstruction of the mass transport channel by virtue of its superior open diffusion pathways.[21] Intensive studies have reported that Cu and Co atoms can significantly mitigate the Fenton effect on stability.[22] As a consequence, it was expected that the ORR electrocatalytic activity would be increased by cooperating TMPs with hollow porous supports.

Herein, we engineered a $Cu_3P$/CoP hybrid embedded in N-doped hollow porous carbon nanospheres using a wet impregnation followed by a pyrolysis-phosphorylation process. The intrinsic activity of the catalyst can be effectively modified by deliberate adjustment of the Co-to-Cu ratio and annealing temperature. The optimized $Cu_3P$/CoP@NC exhibited admirable activity with a half-wave potential ($E_{1/2}$) of 0.82 V and a limiting current density ($j_L$) of 5.07 mA $cm^{-2}$ in the 0.1 M KOH electrolyte. The catalytic performance was on par with those of transition-metal-based materials and commercial Pt/C. This similarity can be attributed to the faster ORR kinetics induced by the synergistic interplay between the bimetal species. Moreover, the hollow porous spherical architecture improves the channels and three-phase interface for mass/electron transfer, thereby bolstering reaction kinetics. Density functional theory (DFT) simulations further indicated that the synergism between $Cu_3P$ and CoP modifies the energy barrier of oxygen-containing intermediates and accelerates electron transport. Predictably, the $Cu_3P$/CoP@NC assembled ZAB demonstrated robust cycling stability over 317 h, narrow voltage gap, discharge specific capacity of 765.6 mAh $g^{-1}$, and high peak power density (209.0 mW $cm^{-2}$), corroborating its promise for application in burgeoning energy conversion devices.

## RESULTS AND DISCUSSION

The reaction's microenvironment at the three-phase interface of the catalyst−electrolyte−oxygen was pivotal for enhancing ORR catalytic capacity. Therefore, hollow porous structural materials with increased exposure to active sites were fabricated by templating methods. The design strategy of $Cu_3P$/CoP@NC is depicted in Figure 1. The presynthesized

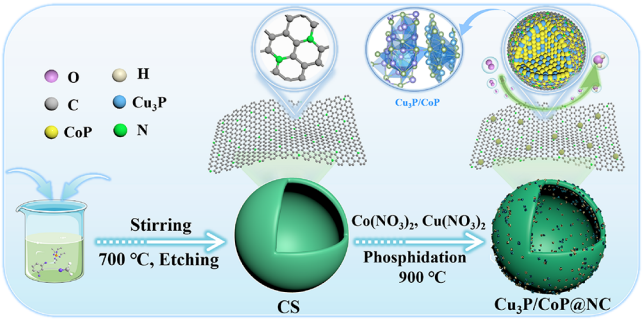


**Figure 1. Synthetic illustration of the $Cu_3P$/CoP@NC synthesis.**

carbon spheres CS with a hollow porous structure were ultrasonically dispersed in the mixture of $Cu(NO_3)_2{\cdot}3H_2O$, $Co(NO_3)_2{\cdot}6H_2O$, and 2-MIM. Following this, the Cu/Co species were adhered to CS after coordinating with 2-MIM. After that, the attached species were encapsulated on CS by the self-polymerization process of dopamine to prevent agglomeration.[23] The target catalyst was obtained using a high-temperature phosphating strategy, and the phase compositions were investigated via powder X-ray diffraction (XRD). The patterns exhibit intense and sharp peaks that align with the diagnostic peaks of orthorhombic CoP (JCPDS: 29-0497) and hexagonal $Cu_3P$ (JCPDS: 02-1263), confirming the successful construction of $Cu_3P$/CoP hybrids with high crystallinity and purity on carbon spheres (Figure 2a).[24,25]

Scanning electron microscopy (SEM) and transmission electron microscopy (TEM) are useful techniques for investigating the microstructure of electrocatalysts. As illustrated in Figure S1, the CS support exhibits a hollow spherical structure with crackle after eliminating $SiO_2$, suggesting the existence of porosity. This was further illuminated by the TEM image, where the shell thickness of CS was measured to be approximately 4.6 nm (Figure 2b). Figure 2c,d confirm that the well-defined hollow spherical morphology with a rough shell was still maintained after anchoring $Cu_3P$/CoP on CS. Contrarily, the thickness of the shell enlarges to 5.8 nm. The hollow porous texture with exposed internal and external surfaces was expected to enhance the accessibility of the active sites and expedite mass transport transfer kinetics.[26,27] The high-resolution TEM (HR-TEM) image and the corresponding lattice spacing profiles of $Cu_3P$/CoP@NC are exhibited in Figure 2e. The visible lattice fringes and uniform lattice spacing distribution are observed, where the interplanar spacing of 0.248 and 0.189 nm can be attributed to the (112) and (211) plane of $Cu_3P$ and CoP, respectively. Figure S2 also substantiates that $Cu_3P$/CoP was encapsulated by graphene layers, which can mitigate agglomeration and corrosion during the electrochemical process, thus boosting the catalyst's stability.[28] The $N_2$ adsorption−desorption isotherm indicates a type IV with a distinctly hysteresis loop, suggesting the existence of a mesoporous structure in the composite (Figure 2f and Figure S3).[29] The formation of porosity originates from extracting $SiO_2$ cores in the support. The specific surface area of $Cu_3P$/CoP@NC was determined to be 155.8 $m^2$ $g^{-1}$ by using Brunauer−Emmett−Teller (BET). The pore distribution curve provides evidence that $Cu_3P$/CoP@NC predominantly exhibits a mesoporous structure, with an average pore size of 7.1 nm. A vivid schematic of the structure is provided in the inset. The high specific surface area and mesoporous structure of $Cu_3P$/CoP@NC were favorable for balancing the electrolyte permeation and ion diffusion, thus accelerating the reaction kinetics.[30,31] Furthermore, energy-dispersive X-ray spectroscopy (EDS) demonstrated the existence of Cu, Co, P, and N elements (Figure S4). As indicated in Figure 2g, the hollow architecture of $Cu_3P$/CoP@NC was further verified by high-angle annular dark-field scanning transmission electron microscopy (HAADF-STEM). The corresponding elemental mappings displayed that C and N were homogeneously distributed, whereas the discrete properties of Cu, Co, and P elements were similar in overall $Cu_3P$/CoP@NC. This result certifies the good incorporation of $Cu_3P$ and CoP species in the CS, as exemplified by XRD analysis.

The ORR process involves intricate electrochemical reactions at gas−liquid−solid three-phase interfaces. Thereinto, the superhydrophobic surface facilitates the capture and diffusion of oxygen while impeding electrolyte transport and diminishes the influx of $OH^-$ to the catalyst surface. Conversely, the superhydrophilic surface hinders the contact between $O_2$ and the active sites, inhibiting the catalyst's activity.[32] Therefore, optimizing the wettability can enhance


https://doi.org/10.1021/acsnano.4c04479
ACS Nano 2024, 18, 17901−17912

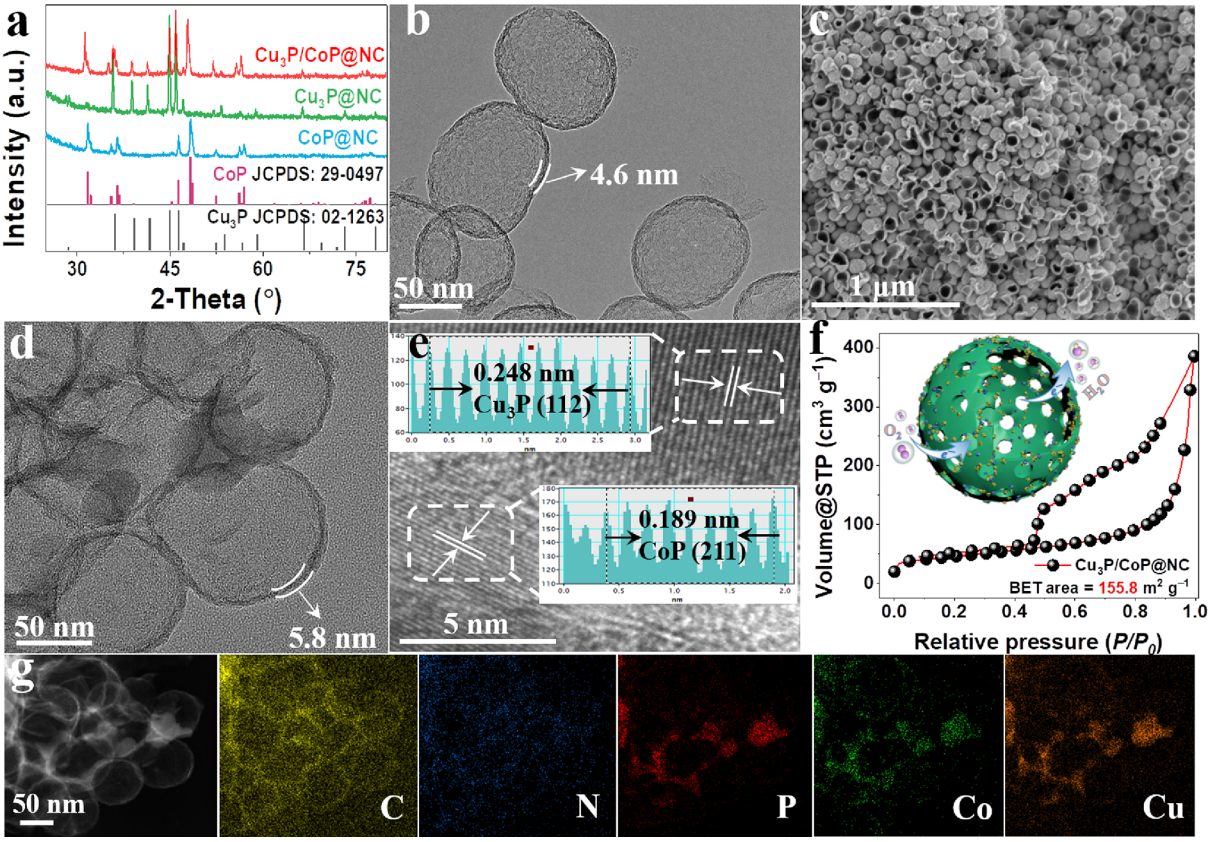


**Figure 2. Morphological and structural characterizations of catalysts. (a) XRD patterns. (b) TEM image of the CS. (c) SEM, (d) TEM, and (e) HR-TEM images and the lattice spacing profiles of the white dotted line regions. (f) $N_2$ adsorption−desorption isotherms (inset: illustration for $Cu_3P$/CoP@NC with hollow mesoporous structure). (g) HAADF-STEM image and corresponding elemental mappings of $Cu_3P$/CoP@NC.**

the ORR activity. The liquid contact angle (CA) was worth considering in the assessment of wettability. $Cu_3P$/CoP@NC (20.6°) offers a lower CA than those of $Cu_3P$@NC (26.2°) and CoP@NC (21.9°), signifying that the composite material has desirable surface wettability and hydrophilic characteristics (Figure 3a).[33] Consequently, the electrolyte readily permeated the pore structure to promote the adsorption of $OH^-$ and ultimately expedite the ORR kinetics.[34] Furthermore, the structural information on catalysts was revealed by Raman spectra. As illustrated in Figure 3b, the G and D bands were associated with graphitic $sp^2$ and defect/disordered $sp^3$ carbon, respectively. The intensity ratio ($I_D/I_G$) was applied to estimate the degree of defects and graphitization within the material.[3] The $I_D/I_G$ value of $Cu_3P$/CoP@NC (1.14) surpasses those of CoP@NC (1.00) and $Cu_3P$@NC (1.03). As a result, the coupling of $Cu_3P$ and CoP probably gives rise to the formation of more disordered/defective carbon, thereby encouraging electrocatalytic activity.[35,36] The elemental composition and chemical states were investigated by using X-ray photoelectron spectroscopy (XPS). As presented in Figure S5a, the XPS survey spectra displayed the characteristic peaks of Cu, Co, P, and N elements in the electrocatalyst, aligning with the mapping results. Moreover, the high-resolution C 1*s* spectra of $Cu_3P$/CoP@NC, $Cu_3P$@NC, and CoP@NC can be split into four peaks: C═C (284.0 eV), C−C (284.8 eV), C−O/C−N (286.0 eV) and O−C═O (288.2 eV), operating as the calibration standard for other XPS spectra (Figure S5b−d).[37] The instrument error was negligible. In Figure S6, the N 1*s* spectra of different materials illustrated the predominance of pyridine N (398.5 eV) and graphitic N (401.0 eV), which was expected to enhance ORR activity.[38] The relative contents of diverse nitrogen species are summarized in Figure 3c by fitting the high-resolution N 1*s* peak areas. $Cu_3P$/CoP@NC had a marginally higher graphitic-N percentage than $Cu_3P$@NC and CoP@NC, which was conducive to enhance the diffusion-limited performance of composites.[39] The Cu 2*p* spectra of $Cu_3P$/CoP@NC were separated into four fractions at 932.6, 934.0, 939.8, and 944.0 eV, corresponding to Cu−P and Cu−O bonds and two satellite peaks, respectively (Figure 3d).[40,41] The existence of the Cu−O bond stems from the surface oxidation of $Cu_3P$.[42] The binding energy of the Cu−P bond in $Cu_3P$/CoP@NC exhibited a positive shift of 0.1 eV relative to $Cu_3P$@NC, indicating that Cu ions have lost electrons. Additionally, as observed in the inset of Figure 3d, the Auger electron spectroscopy (AES) indicated the presence of $Cu^+$.[43] Meanwhile, a higher ratio of $Cu^+$ to $Cu^{2+}$ was propitious to oxygen binding and activation; thereby, $Cu_3P$/CoP@NC possesses a biggish potentiality to promote ORR activity.[44] The Co 2*p* region of $Cu_3P$/CoP@NC confirmed that the peaks centered on 778.5/793.5, 781.2/798.5, and 785.0/804.8 eV belong to Co−P and Co−O bonds and satellite peaks, respectively (Figure 3e).[24,45] Analogously, the binding energy of the Co−P bond underwent a positive shift of 0.1 eV relative to CoP@NC. The above results indicate that the formation of composites results in surface electron reconstruction of metal centers.[46] The P 2*p* spectra of different catalyst were compared in Figure 3f, in which deconvolution three component peaks at


https://doi.org/10.1021/acsnano.4c04479
ACS Nano 2024, 18, 17901−17912

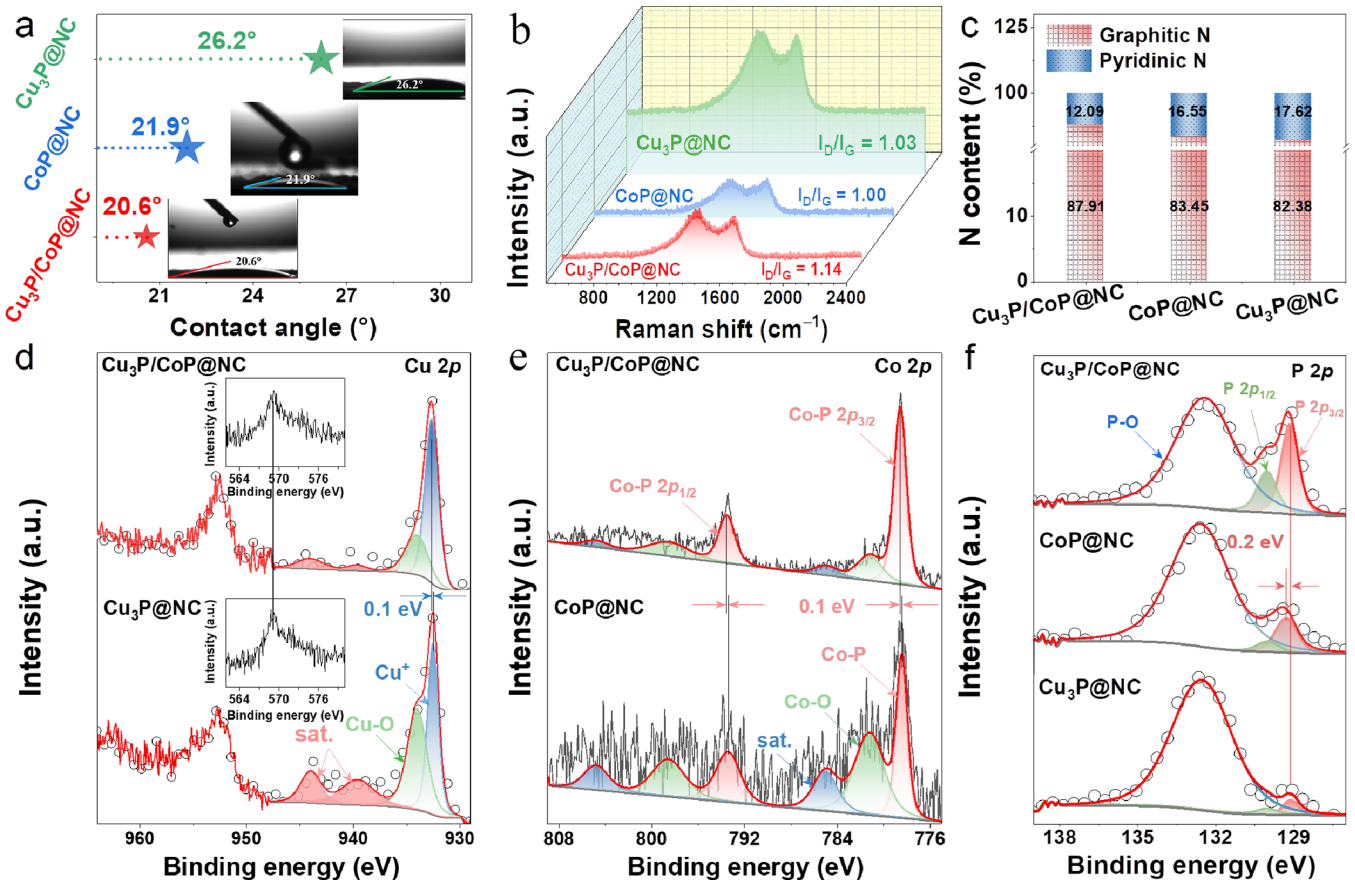


**Figure 3. (a) Bubble contact angle images of different catalysts. (b) Raman spectra. (c) The relative contents of different N species. High-resolution (d) Cu 2*p*, (e) Co 2*p*, and (f) P 2*p* XPS spectra for $Cu_3P$/CoP@NC, $Cu_3P$ @NC, and CoP@NC.**

around 129.2, 130.0, and 132.4 eV were ascribed to $2p_{3/2}$ and $2p_{1/2}$ of P−M and P−O bond, respectively.[47] The P−O bond primarily originates from the surface oxidation of materials.[48] Compared to CoP@NC, the P 2*p* binding energy of $Cu_3P$/CoP@NC was negatively shifted by about 0.2 eV. Evidently, the partial electron transfer from metal to P can induce the strong chemical interaction, thence endowing the catalyst with fast mass transfer rate and reaction kinetics.[49] As a result, the proportions of Co−P, Cu−P, and metal−P bonds were increased in $Cu_3P$/CoP@NC. Notably, the enumerated results further point out the successful preparation of the $Cu_3P$/CoP hybrid on hollow porous CS, which was in conformity with the TEM and XRD analysis.

The pristine catalytic performance of the as-synthesized catalysts was estimated by cyclic voltammetry (CV) and linear sweep voltammetry (LSV) in $N_2$- and $O_2$-saturated 0.1 M KOH media. As shown in Figures S7 and S8, the optimal synthesis conditions were explored by adjusting the pyrolysis temperature and metal ratio during the preparation. The corresponding ring currents are presented in Figure S9a,b. It was found that the catalyst exhibited the highest $j_L$ and $E_{1/2}$ and a lower Tafel slope at a high temperature of 900 °C. Meanwhile, the lower $H_2O_2$ yield affirmed that the reaction was closer to the four-electron transfer process. The Cu/Co stoichiometric ratios were simultaneously adjusted to comprehend the implication on ORR performance. The experiments revealed that a Co/Cu molar ratio of 7:3 surpassed a ratio of 1:9 in terms of catalytic activity. And the performance of the catalysts was significantly enhanced with a ratio of 8:2 compared to a ratio of 2:8. This result confirms that Co species serves as the primary active sites during the ORR process. The corresponding values, as summarized in Figure S10, certify that $Cu_3P$/CoP@NC (900 °C) can provide a higher intrinsic activity. The inductively coupled plasma mass spectrometry (ICP-MS) measurements in Table S1 indicate a Co content as high as 14.03% at a ratio of 7:3, further inferring the predominance of Co species in the electrocatalytic process. Nevertheless, the catalyst exhibited superb activity at a molar ratio of 1:1. Although the catalyst's performance was slightly lower than 1:1 at a Co to Cu ratio of 6:4, it was better than the ratios of 8:2, 2:8, and 1:9, confirming that the ORR activities were driven by the interaction between two species. The above results show that the optimal catalyst, denoted as $Cu_3P$/CoP@NC, was obtained at Co/Cu = 1:1 and an annealing temperature of 900 °C.

As revealed in Figure 4a, CV curves reflected that there was a prominent cathodic peak in the $O_2$-purged solution rather than $N_2$-saturated one, validating the effectiveness of the fabricated catalyst for ORR.[50] The observed similarity in the CV curves of $Cu_3P$/CoP@NC and CoP@NC was attributed to certain structural and chemical characteristics of CoP as the main active species, which were also confirmed by the following discussion. Notably, the observed peaks between 0.3 and 0.4 V (vs RHE) on the CV curve of commercial Pt/C originate from the adsorption and desorption of hydrogen at Pt sites.[51] Furthermore, the kinetic properties and catalytic activities of all materials were unveiled by the LSV polarization curves (Figure 4b). $Cu_3P$/CoP@NC affords superior ORR


https://doi.org/10.1021/acsnano.4c04479
ACS Nano 2024, 18, 17901−17912

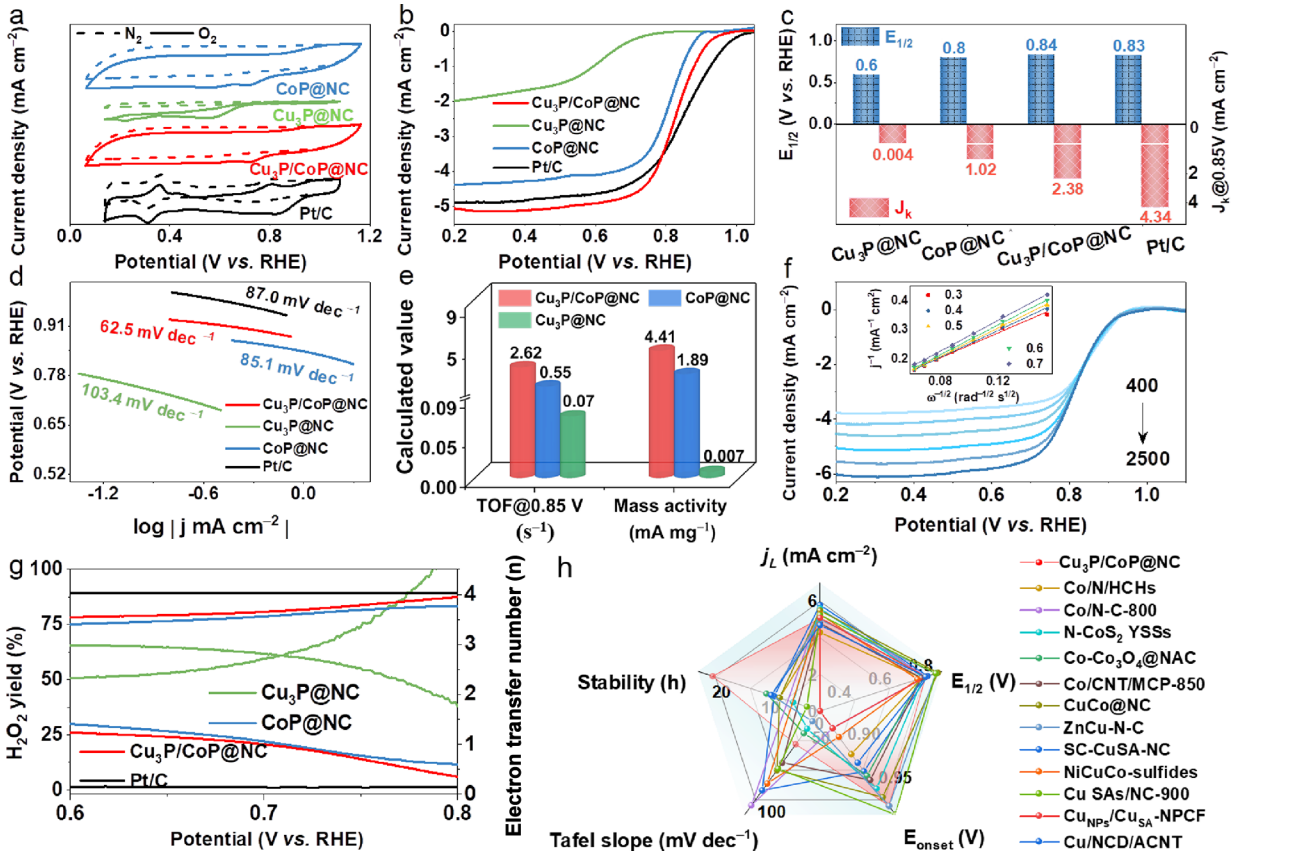


**Figure 4. Electrocatalytic ORR activity. (a) CV, (b) LSV polarization curves and (c) $j_k$ (0.85 V vs RHE) and $E_{1/2}$ of as-prepared catalysts. (d) Corresponding Tafel slope plots. (e) TOF and mass activity at 0.85 V. (f) LSV curves of $Cu_3P$/CoP@NC at various rotation rates and K−L plots (inset). (g) $H_2O_2$ yield (%) and electron transfer number ($n$). (h) Comparison of the ORR activity of $Cu_3P$/CoP@NC with recently reported Co- or Cu-based materials.**

performance with an $E_{1/2}$ of 0.82 V and $j_L$ of 5.07 mA cm$^{-2}$. These results evidently outperform $Cu_3P$@NC (0.60 V, 1.99 mA cm$^{-2}$) and CoP@NC (0.80 V, 4.37 mA cm$^{-2}$) and were analogous to those of the benchmark Pt/C (0.83 V, 4.89 mA cm$^{-2}$). As portrayed in Figure 4c, the kinetic current densities ($j_k$'s) were calculated to have a better insight on the effects of reaction kinetics and mass transfer processes on catalyst activity. The $j_k$ of $Cu_3P$/CoP@NC was 2.38 mA cm$^{-2}$ at a potential of 0.85 V, overwhelmingly exceeding those of $Cu_3P$@NC (0.004 mA cm$^{-2}$) and CoP @NC (1.02 mA cm$^{-2}$) but slightly lower than that of Pt/C (4.34 mA cm$^{-2}$). The fast reaction kinetics of $Cu_3P$/CoP@NC was also supported via a small Tafel slope of 62.5 mV dec$^{-1}$ (Figure 4d). The hollow mesoporous structure of $Cu_3P$/CoP@NC provides channels for mass transport and endows the catalyst with faster kinetics.[52] Notably, CoP@NC has significantly higher performance than that of $Cu_3P$@NC, reaffirming that CoP is considered as a more powerful promoter and $Cu_3P$ as an auxiliary. The impressive catalytic activity of $Cu_3P$/CoP@NC was ascribed to the synergism between $Cu_3P$ and CoP species, resonating with the optimized procedure and the ICP-MS findings. The turnover frequency (TOF) and mass activity (MA) were practical indicators to gain insight into intrinsic activity, which hypothesized that all metal atoms were treated as active centers in catalysts. Figure 4e describes that the MA of $Cu_3P$/CoP@NC (4.41 mA mg$^{-1}$) surpasses those of CoP@NC (1.89 mA mg$^{-1}$) and $Cu_3P$@NC (0.007 mA mg$^{-1}$), which was ascribed to the cooperation of bimetal and support bringing about a substantial proportion of active sites.[53] $Cu_3P$/CoP@NC achieves the highest TOF of 2.62 s$^{-1}$ at 0.85 V, underscoring the benefits brought by the holistic structural optimization.[53] To thoroughly explicate the superiority of $Cu_3P$/CoP@NC, LSV curves indicate the incremental limiting current density based on various rotational speeds (400−2025 rpm) due to different mass transfer rates (Figure 4f). The associated Koutecky−Levich (K−L) plots illustrate a keen linearity, indicating a first-order reaction kinetics feature in ORR (inset in Figure 4f).[54] Besides, the calculated electron transfer number ($n$) for each oxygen molecule was close to 4, as evidenced by rotating ring disk technology. The correlative ring currents of various catalysts are displayed in Figure S9c. The content of $H_2O_2$ species with regard to total $O_2$ reduction products of $Cu_3P$/CoP@NC remained below 25% in the potential windows of 0.6−0.8 V (vs RHE), disclosing that $O_2$ was reduced to $H_2O$ via a four-electron pathway (Figure 4g). Significantly, after the electrocatalytic reaction, the characteristic diffraction peaks of $Cu_3P$ and CoP still existed in the catalyst, and no metals in other valence states were generated, as confirmed by the XRD pattern and XPS spectra (Figures S11 and S12). These findings indicate that the catalyst maintains a stable structure without reconstruction during the electrocatalytic process. Therefore, $Cu_3P$/CoP@NC has potential application prospects in ZAB. As anticipated, the ORR activity of $Cu_3P$/CoP@NC was comparable to those of some Co- or Cu-based catalysts (Figure 4h and Table S2) owing to an open architecture with hollow mesopores that


https://doi.org/10.1021/acsnano.4c04479
ACS Nano 2024, 18, 17901−17912

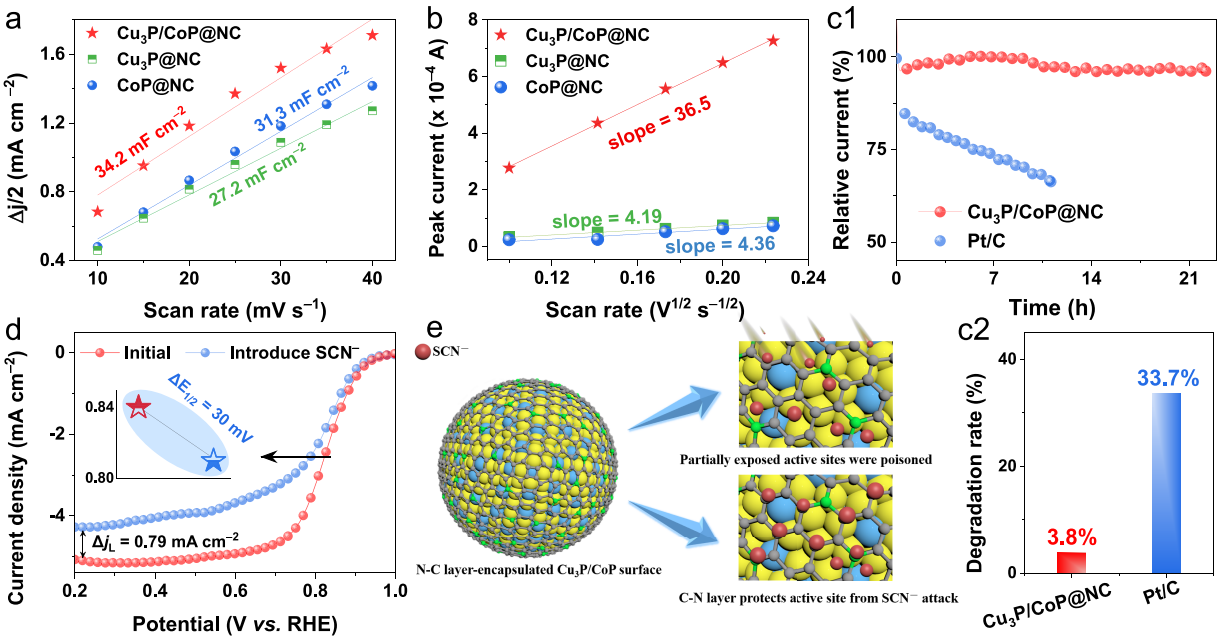


**Figure 5.** (a) $C_{dl}$ values of $Cu_3P$/CoP@NC, $Cu_3P$@NC, and CoP@NC. (b) CV fitting curves in the mixed solution of 0.1 M KCl and 5 mM $K_3[Fe(CN)_6]$ at various scan rates. (c1) Stability test of $Cu_3P$/MoP@C and Pt/C (20 wt %) in 0.1 M KOH at a rotating speed of 1600 rpm and (c2) the current degradation rate after the durability test. (d) LSV curves of $Cu_3P$/CoP@NC before and after KSCN poisoning measurement. (e) Schematic diagram of a probable mechanism for $SCN^-$ poisoning experiment on $Cu_3P$/CoP@NC together with the authentication of the active site.

facilitates exposed active area and mass transport improvement.

To uncover the pristine electrocatalytic activity for $Cu_3P$/CoP@NC, the electrochemical surface area (ECSA) was assessed through double-layer capacitance ($C_{dl}$) calculations in the non-Faradaic region (Figure 5a and Figure S13). $Cu_3P$/CoP@NC has a higher $C_{dl}$ value than single metal catalysts, inferring that the spherical framework with hollow mesopores can furnish an abundance of active sites to boost the ORR reaction.[55] Generally, CV curves were captured in a mixed solution of 0.1 M KCl and 0.5 mM $K_3[Fe(CN)_6]$ at various scan rates (Figure S14). The resulting fitted line was in accordance with the $C_{dl}$ trend, further emphasizing the accessibility of the $Cu_3P$/CoP@NC active site density (Figure 5b). The concurrent long-term stability and methanol tolerance were tested to estimate the practical application of $Cu_3P$/CoP@NC (Figure S15 and Figure 5c1). Compared to the benchmark Pt/C (81.7%), $Cu_3P$/CoP@NC retains 94.5% of the initial current density with the lowest disturbance following 3 M methanol injection, unveiling that $Cu_3P$/CoP@NC exhibits compelling methanol tolerance. Likewise, $Cu_3P$/CoP@NC persists in exceptional stability with a current density degradation rate of 3.8% over a prolonged 22 h period of current−time measurements. In comparison, the current density of Pt/C decayed by up to 33.7% after 11 h (Figure 5c2). As shown in the aforementioned data, the extraordinary stability corroborated the fact that the carbon skeleton effectively alleviates the dissolution and aggregation of metal ions.[56] Additionally, the bimetallic synergism and carbon surfaces were prone to resist external interference.[34] The thiocyanide anions ($SCN^-$) were regarded as a probe to discriminate the activity centers, as they readily form complexation with various metal species (such as Fe, Co, and Cu) (Figure 5d). As shown in Figure 5e, C atoms of the graphene shell fail to entirely cover the metal site's surface due to different atomic radii.[57] A fraction of the exposed sites may be poisoned by $SCN^-$ anions, blocking them from interacting with oxygen feedstock. Consequently, $Cu_3P$/CoP@NC showed a deactivation phenomenon with a drop in $E_{1/2}$ and $j_L$ ($\Delta E_{1/2}$ = 30 mV and $\Delta j_L$ = 0.79 mA $cm^{-2}$) upon introducing $SCN^-$ ions, elucidating that the crucial active centers responsible for the catalytic performance were the metal species.[12,58]

To explicate the relationship between the enhanced ORR activity and the interface electronic interaction of $Cu_3P$/CoP, DFT calculations were introduced for the optimized model structures (Figure 6a and Figure S16). From Figures 6b and Figure S17, the charge density difference exhibits palpable electron enrichment at the interfaces of the $Cu_3P$ and CoP species. It was intriguing that the electron deficiency of the Cu center was more than that of Co at the interface, indicating that Cu sites function as modulators.[59] The charge accumulation and depletion zones are depicted more pictorially in Figure 6c. The calculated projected density of states (PDOS) is shown in Figure 6d. Apparently, $Cu_3P$/CoP and CoP exhibit a higher electron density distribution around the Fermi level ($E_f$) than $Cu_3P$, resulting in superior conductivity to ensure fast electron transfer. Additionally, PDOS near the $E_f$ of $Cu_3P$/CoP basically derives from the Cu 3*d* and Co 3*d* orbitals, implying Cu and Co as electron donors. Contrarily, the P 2*p* orbital of $Cu_3P$/CoP and CoP was apart from the $E_f$ and primarily situated at a place with substantially lower energy, pointing that P species act as electron acceptors.[60] The findings demonstrate the significant charge interaction among Cu, Co, and P atoms, congruent with the XPS results. Critically, the interfacial electronic interaction can engineer the position of the *d*-band center ($\varepsilon_d$), allowing for the tailored adsorption energy of oxygen-containing intermediates.[61] Figure 6e provides an intuitive representation of $\varepsilon_d$ for $Cu_3P$/CoP, $Cu_3P$, and CoP. Specifically, the $\varepsilon_d$ values for


https://doi.org/10.1021/acsnano.4c04479
ACS Nano 2024, 18, 17901−17912

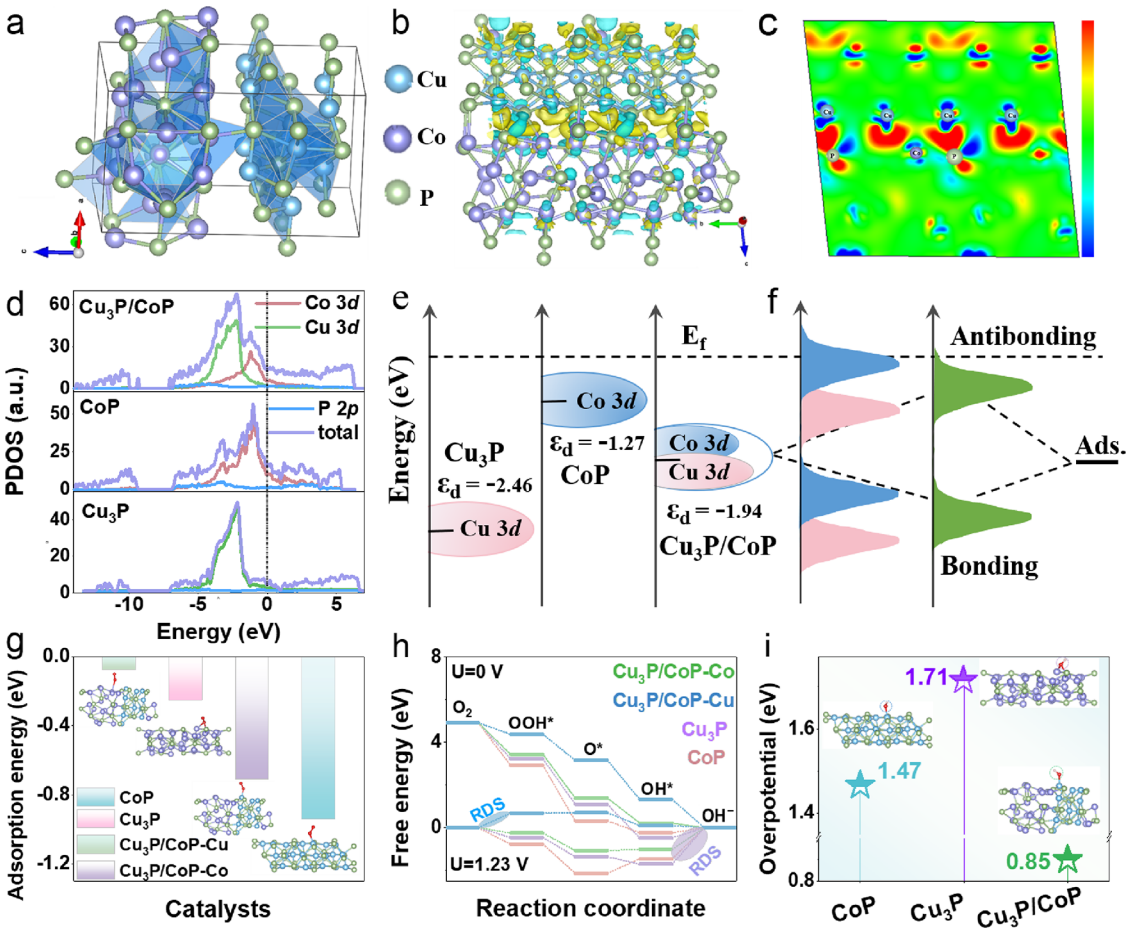


**Figure 6. (a) Optimized model configuration, (b) charge density difference of $Cu_3P$/CoP (the yellow and cyan areas display the accumulation and depletion of charges, respectively), and (c) cross-sectional diagram. (d) PDOS plots for $Cu_3P$, CoP, and $Cu_3P$/CoP. (e) Schematic illustration of the *d*-band center as well as (f) the corresponding diagram of bond formation between the catalyst surface and adsorbate. (g) Adsorption energy of the $O_2$ and (h) Gibbs free energy profiles for $Cu_3P$, CoP, $Cu_3P$/CoP-Cu, and $Cu_3P$/CoP-Co. (i) Overpotential of electrocatalysts. $Cu_3P$/CoP-Cu and $Cu_3P$/CoP-Co represent Cu and Co sites in the $Cu_3P$/CoP catalyst, respectively.**

CoP and $Cu_3P$ were −1.27 and −2.46 eV, respectively, whereas $Cu_3P$/CoP exhibited a value of −1.94 eV. The data convey that the antibonding energy states were either too high or too low in CoP and $Cu_3P$. The antibonding state was more difficult or easier to be filled after the hybridization of catalysts with the adsorbate, resulting in a stronger or weaker bonding affinity between the catalysts and adsorbate (Figure 6f). Consequently, this variation renders the adsorbate more difficult to desorb or adsorb, resulting in undesirable ORR activity in CoP and $Cu_3P$. $Cu_3P$/CoP exhibited moderate antibonding energy states, optimizing the adsorption force of intermediates. Hence, the improvement of the ORR activity of $Cu_3P$/CoP was primarily credited to the valid regulation of Cu species. To this end, as depicted in Figure 6g, $Cu_3P$ and CoP exhibited either excessively weak or strong adsorption energies, resulting in hindered adsorption or desorption of $O_2$, respectively. Cu sites encouraged the desorption of $O_2$ from the catalyst surface owing to their smaller adsorption energy. The results indicate that the incorporation of Cu species optimizes the electronic structure of Co sites, resulting in favorable ORR kinetics.[62] The mechanism associated with the $4e^-$ transfer pathway was investigated by analyzing the intermediate free energy on different models (Figure S18). All reaction steps were uncovered to be energetically downhill at an equilibrium potential ($U$) of 0 V, confirming their spontaneous and exothermic nature (Figure 6h). At $U$ = 1.23 V, the rate-determining steps (RDS) for $Cu_3P$/CoP-Cu was the formation of OOH* ($O_2 + H_2O + e^- \rightarrow OOH^* + OH^-$). Dissimilarly, $Cu_3P$/CoP-Co, $Cu_3P$, and CoP exhibit the same RDS during the step of *OH dissociation ($OH^* + e^- \rightarrow OH^-$). The strong bonding of OH* on active sites drastically restricted the progression of the reaction. A substantially lower energy barrier was observed for $Cu_3P$/CoP-Co, denoting that the incorporation of Cu favors the release of OH* and accelerates the reaction kinetics. Simultaneously, the free energy of Cu and Co sites in $Cu_3P$/CoP was calculated to discriminate the active center. The main active centers were determined to be the Co sites because OH* dissociation in CoP was lower compared to that in $Cu_3P$. Quantitatively, $Cu_3P$/CoP exhibited a lower overpotential of 0.85 eV than those of $Cu_3P$ (1.71 eV) and CoP (1.47 eV), corroborating its favorable kinetics (Figure 6i). The DFT analysis aligns with the experimental results. The strong interaction between Cu and Co significantly reduces the reaction barrier and facilitates electron transfer, governing the fascinating ORR activity of $Cu_3P$/CoP.

Considering the admirable ORR electrocatalytic capability of $Cu_3P$/CoP@NC, ZAB was fabricated to explore its viability in actual energy conversion devices. Figure 7a presents the schematic construction of ZAB, whose energy was derived


https://doi.org/10.1021/acsnano.4c04479
ACS Nano 2024, 18, 17901−17912

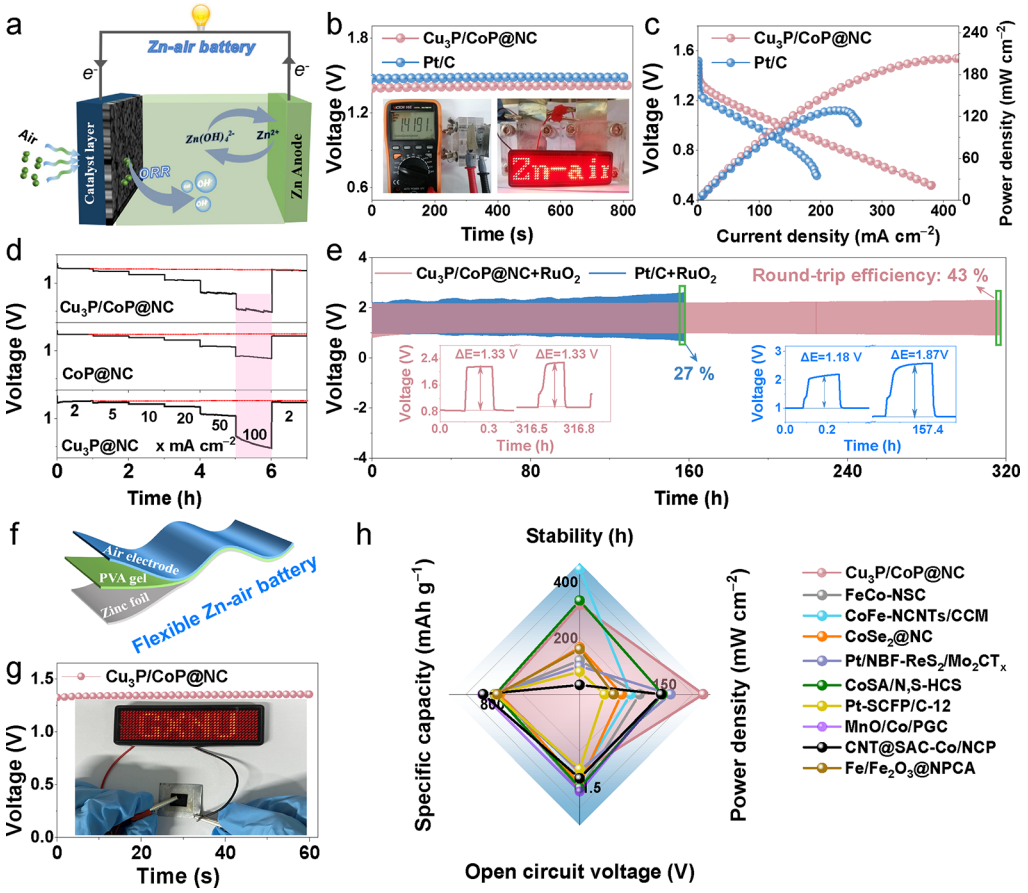


**Figure 7. (a) Schematic configuration of the self-assembled ZAB. (b) OCV plots (inset: an optical image for OCV measured by a multimeter and an LED screen lit up by two ZAB connected in series). (c) Discharge polarization curves and power densities. (d) Discharge curves at various current densities and each step lasting for 60 min (*x* was different current density values: 2−100 mA cm$^{-2}$). (e) Charge−discharge cycle curves at a current density of 5 mA cm$^{-2}$. (f) Schematic diagram and (g) OCV of flexible ZAB. Inset: photograph of an LED plane illuminated by a flexible ZAB. (h) $Cu_3P$/CoP@NC as an air cathode vs recently reported catalysts in the literature.**

from the redox reaction of the oxygen feedstock. As illustrated in Figure 7b, $Cu_3P$/CoP@NC-based ZAB yielded an open-circuit voltage (OCV) of 1.42 V comparable to Pt/C (1.49 V), which accorded well with the multimeter test result. The high OCV derives from the distinguished catalytic performance and conductivity of $Cu_3P$/CoP@NC. Synchronously, two ZABs integrated into a series circuit can successfully power an LED plate with a voltage of about 3 V (inset in Figure 7b), declaring the promising practicability of $Cu_3P$/CoP@NC. Figure 7c shows that the $Cu_3P$/CoP@NC-equipped ZAB unfolds a preeminent peak power density of 209.0 mW cm$^{-2}$, significantly surpassing that of the benchmark Pt/C (133.5 mW cm$^{-2}$). Furthermore, $Cu_3P$/CoP@NC affords a gratifying specific capacity of 765.6 mAh g$^{-1}$ at a discharge current density of 10 mA cm$^{-2}$, reaching ∼93.4% of the theoretical capacity utilization (820 mAh g$^{-1}$) (Figure S19). The discharge rate performance of $Cu_3P$/CoP@NC, CoP@NC, and $Cu_3P$@NC-equipped ZAB at various galvanostatic current density is provided in Figure 7d. The $Cu_3P$/CoP@NC-based ZAB was barely subjected to a voltage decline during a series of discharge quizzes. However, $Cu_3P$@NC-based ZAB exhibited a voltage decay at a current density of 100 mA cm$^{-2}$. Interestingly, the discharge voltage of $Cu_3P$/CoP@NC-based ZAB was reversibly returned to the initial level as the current density was restored to 2 mA cm$^{-2}$. In contrast, the voltage of $Cu_3P$@NC- and CoP@NC-based ZAB was not recovered, thereby endorsing the splendid rate capability of $Cu_3P$/CoP@NC-based ZAB. Surprisingly, the $Cu_3P$/CoP@NC + $RuO_2$-based ZAB exhibits a long lifespan of over 317 h with a scarcely fading charge−discharge voltage gap ($\Delta E$) during operation. Also, the round-trip efficiency still remained at 43% even after the 317 h cycle. Conversely, the $\Delta E$ of the Pt/C + $RuO_2$ couple remarkably rose from 1.18 to 1.87 V and the round-trip efficiency dropped to 27% after a cycle of only 158 h. This finding signified that $Cu_3P$/CoP@NC + $RuO_2$-based ZAB possesses brilliant durability, manifesting the exploitability of $Cu_3P$/CoP@NC in ZAB (Figure 7e). To validate the application potential of $Cu_3P$/CoP@NC-based ZAB as a flexible energy storage/conversion device. Figure 7f fairly presents a schematic of self-assembling flexible ZAB employing poly(vinyl alcohol) (PVA) hydrogel as a solid electrolyte. The $Cu_3P$/CoP@NC-based flexible ZAB achieved an OCV of 1.35 V while being tested at bending angles of 0, 30, 90, and 180° to trial flexibility (Figures 7g and Figure 20). The difference in the OCV of flexible ZAB at various bending angles was insignificant. The result displays that the hollow nanomicrospheres of $Cu_3P$/CoP@NC have favorable chemical and structural stability. Interestingly, the LED plate can be powered by a $Cu_3P$/CoP@NC-based flexible ZAB (inset in Figure 6g), demonstrating its good practical application prospect. Notably, the catalytic ability of $Cu_3P$/CoP@NC rivaled those of Pt/C and other recently reported materials in ZABs (Figure 7h),


https://doi.org/10.1021/acsnano.4c04479
ACS Nano 2024, 18, 17901−17912

ensuring that $Cu_3P$/CoP@NC can be a competitive candidate for actual energy conversion devices.

Taken in aggregate, the following merits were disclosed to be responsible for the satisfactory ORR activity of $Cu_3P$/CoP@NC: (i) The enlargement of the specific surface area was rendered by the hollow mesoporous architecture, allowing $Cu_3P$/CoP@NC to expose valid active center.[63,64] (ii) The connected inner and outer walls supply a channel for electrolyte permeability and electron/ion transfer, resulting in faster reaction kinetics.[65] (iii) The N-doped porous carbon matrix can effectively mitigate metal active center dissolution and agglomeration to boost the corrosion resistance of electrocatalyst.[66] (iv) The synergistic interaction between Cu and Co species diminishes the reaction barrier, conferring fast ORR kinetics.[67]

## CONCLUSIONS

In a nutshell, we have constructed a $Cu_3P$/CoP@NC electrocatalyst with a hollow mesoporous spherical structure by polymerization and a high-temperature treatment process and investigated its intrinsic ORR activity in alkaline conditions. The catalytic performance and endurance of $Cu_3P$/CoP@NC exceed those of monometallic materials and rival those of the benchmark Pt/C, endowing it with promise as an air cathode catalyst in ZAB. Systematic electrochemical studies and various characterization techniques established that the superior ORR activity was predominated by an exotic hollow mesoporous architecture and the synergism between $Cu_3P$ and CoP species. Furthermore, the N doping further improves the diffusion-limited properties. The $Cu_3P$/CoP@NC-based ZAB achieves a preeminent power density of 209.0 mW $cm^{-2}$ and splendid cycling stability of over 317 h. Meanwhile, the flexible ZAB manifests wonderful flexibility and practical application potential. Overall, this work offers a valuable and nontoxic guideline for constructing hollow mesoporous structure composites for next-generation energy conversion devices.

## EXPERIMENTAL SECTION

**Synthesis of Hollow Porous Carbon Nanospheres.** Carbon nanospheres were prepared according to our previously reported work.[25]

**Synthesis of $Cu_3P$/CoP@NC.** $Cu_3P$/CoP@NC was fabricated by employing hollow porous carbon nanospheres as a support. Certain amounts of carbon nanospheres, $Cu(NO_3)_2{\cdot}3H_2O$, and $Co(NO_3)_2{\cdot}6H_2O$ were dispersed in 30 mL of ethanol through ultrasonication for 30 min to form a solution. Afterward, 0.12 mmol of 2-MIM was added to the above solution and agitated constantly for 6 h. Subsequently, 0.30 mmol of Tris and 0.16 mmol of dopamine hydrochloride were added to the above mixture and continuously stirred for 3 h. The resultant product was gathered by centrifugation and dried in an oven at 60 °C. The precursor powder and red phosphorus (P) were ground uniformly with the mass ratio of 1:2 and pyrolyzed at different temperatures (800, 900, and 1000 °C) for 2 h in a nitrogen atmosphere (5 °C $min^{-1}$).

For comparison, the molar amount of Co/Cu (8:2, 2:8, 6:4, 1:9, and 7:3) was modified to tune the metal doping level during synthesis. $Cu_3P$@NC and CoP@NC as single metal specimens were prepared with the same recipe except without $Co(NO_3)_2{\cdot}6H_2O$ or $Cu(NO_3)_2{\cdot}3H_2O$. Unless otherwise specified, the optimal calcination temperature of $Cu_3P$/CoP@NC was 900 °C and the Co/Cu molar ratio was 1:1.

## ASSOCIATED CONTENT

### Supporting Information

The Supporting Information is available free of charge at https://pubs.acs.org/doi/10.1021/acsnano.4c04479.

Reagents; electrochemical measurements; the details of ZAB's fabrication; materials; characterization; computational methods; supplementary electrochemical data; tables; theoretical calculation models; configurations of intermediates; and specific capacity plots of ZAB (PDF)

## AUTHOR INFORMATION


### Corresponding Author

**Xiulin Yang** − *Guangxi Key Laboratory of Low Carbon Energy Materials, School of Chemistry and Pharmaceutical Sciences, Guangxi Normal University, Guilin 541004, China;* orcid.org/0000-0003-2642-4963; Email: xlyang@gxnu.edu.cn

### Authors

**Man Guo** − *Guangxi Key Laboratory of Low Carbon Energy Materials, School of Chemistry and Pharmaceutical Sciences, Guangxi Normal University, Guilin 541004, China*

**Lixia Wang** − *Guangxi Key Laboratory of Low Carbon Energy Materials, School of Chemistry and Pharmaceutical Sciences, Guangxi Normal University, Guilin 541004, China*

**Zhiyang Huang** − *Guangxi Key Laboratory of Low Carbon Energy Materials, School of Chemistry and Pharmaceutical Sciences, Guangxi Normal University, Guilin 541004, China*

**Huatong Li** − *Guangxi Key Laboratory of Low Carbon Energy Materials, School of Chemistry and Pharmaceutical Sciences, Guangxi Normal University, Guilin 541004, China*

**Tayirjan Taylor Isimjan** − *Saudi Arabia Basic Industries Corporation (SABIC) at King Abdullah University of Science and Technology (KAUST), Thuwal 23955-6900, Saudi Arabia;* orcid.org/0000-0003-1735-481X

Complete contact information is available at: https://pubs.acs.org/10.1021/acsnano.4c04479

### Author Contributions

[§]M.G. and L.W. contributed equally to this work.


### Notes

The authors declare no competing financial interest.

## ACKNOWLEDGMENTS

This work has been supported by the National Natural Science Foundation of China (nos. 52363028 and 21965005), Guangxi Technology Base and Talent Subject (GUIKE AD23023004, GUIKE AD20297039), and Natural Science Foundation of Guangxi Province (2021GXNSFAA076001).

## REFERENCES

(1) Hui, X.; Zhang, P.; Li, J.; Zhao, D.; Li, Z.; Zhang, Z.; Wang, C.; Wang, R.; Yin, L. In Situ Integrating Highly Ionic Conductive LDH-Array@PVA Gel Electrolyte and MXene/Zn Anode for Dendrite-Free High-Performance Flexible Zn−Air Batteries. *Adv. Energy Mater.* **2022**, *12*, 2201393.

(2) Guo, M.; Huang, Z.; Qu, Y.; Wang, L.; Li, H.; Isimjan, T. T.; Yang, X. Synergistic Effect and Nanostructure Engineering of Three-Dimensionally Hollow Mesoporous Spherical $Cu_3P/TiO_2$ in Aqueous/Flexible Zn−Air Batteries. *Appl. Catal. B Environ. Energy* **2023**, *320*, No. 121991.

(3) Li, P.; Wang, H.; Tan, X.; Hu, W.; Huang, M.; Shi, J.; Chen, J.; Liu, S.; Shi, Z.; Li, Z. Bifunctional Electrocatalyst With $CoN_3$ Active

Sties Dispersed on N-Doped Graphitic Carbon Nanosheets for Ultrastable Zn-Air Batteries. *Appl. Catal. B Environ. Energy* **2022**, *316*, No. 121674.
(4) Wagh, N. K.; Shinde, S. S.; Lee, C. H.; Kim, S.-H.; Kim, D.-H.; Um, H.-D.; Lee, S. U.; Lee, J.-H. Supramolecular Polymer Intertwined Free-Standing Bifunctional Membrane Catalysts for All-Temperature Flexible Zn−Air Batteries. *Nano-Micro Lett.* **2022**, *14*, 190.
(5) Chen, Y.; Qiao, S.; Tang, Y.; Du, Y.; Zhang, D.; Wang, W.; Zhang, H.; Sun, X.; Liu, C. Double-Faced Atomic-Level Engineering of Hollow Carbon Nanofibers As Free-Standing Bifunctional Oxygen Electrocatalysts for Flexible Zn−Air Battery. *ACS Nano* **2022**, *16*, 15273−15285.
(6) Thangasamy, P.; Oh, S.; Randriamahazaka, H.; Nam, S.; Oh, I.-K. Mechanistic Insight into Collectively Exhaustive CoPi-NPC Nanosheets for Oxygen Reduction Reaction and Zn-Air Battery. *Appl. Catal. B Environ. Energy* **2022**, *316*, No. 121656.
(7) Sarkar, S.; Biswas, A.; Siddharthan, E. E.; Thapa, R.; Dey, R. S. Strategic Modulation of Target-Specific Isolated Fe,Co Single-Atom Active Sites for Oxygen Electrocatalysis Impacting High Power Zn−Air Battery. *ACS Nano* **2022**, *16*, 7890−7903.
(8) Liu, Y.; Chen, Z.; Li, Z.; Zhao, N.; Xie, Y.; Du, Y.; Xuan, J.; Xiong, D.; Zhou, J.; Cai, L.; Yang, Y. CoNi Nanoalloy-Co-$N_4$ Composite Active Sites Embedded in Hierarchical Porous Carbon As Bi-Functional Catalysts for Flexible Zn-Air Battery. *Nano Energy* **2022**, *99*, No. 107325.
(9) Hou, Z.; Sun, Z.; Cui, C.; Zhu, D.; Yang, Y.; Zhang, T. Ru Coordinated $ZnIn_2S_4$ Triggers Local Lattice-Strain Engineering to Endow High-Efficiency Electrocatalyst for Advanced Zn-Air Batteries. *Adv. Funct. Mater.* **2022**, *32*, 2110572.
(10) Pan, Y.; Ma, X.; Wang, M.; Yang, X.; Liu, S.; Chen, H.; Zhuang, Z.; Zhang, Y.; Cheong, W.; Zhang, C.; Cao, X.; Shen, R.; Xu, Q.; Zhu, W.; Liu, Y.; Wang, X.; Zhang, X.; Yan, W.; Li, J.; Chen, H. M.; Chen, C.; Li, Y.; et al. Construction of N, P Co-Doped Carbon Frames Anchored with Fe Single Atoms and $Fe_2P$ Nanoparticles As a Robust Coupling Catalyst for Electrocatalytic Oxygen Reduction. *Adv. Mater.* **2022**, *34*, 2203621.
(11) He, Y.; Yang, X.; Li, Y.; Liu, L.; Guo, S.; Shu, C.; Liu, F.; Liu, Y.; Tan, Q.; Wu, G. Atomically Dispersed Fe−Co Dual Metal Sites As Bifunctional Oxygen Electrocatalysts for Rechargeable and Flexible Zn−Air Batteries. *ACS catal.* **2022**, *12*, 1216−1227.
(12) Chen, S.; Luo, T.; Li, X.; Chen, K.; Fu, J.; Liu, K.; Cai, C.; Wang, Q.; Li, H.; Chen, Y.; Ma, C.; Zhu, L.; Lu, Y.-R.; Chan, T.-S.; Zhu, M.; Cortés, E.; Liu, M. Identification of the Highly Active Co−$N_4$ Coordination Motif for Selective Oxygen Reduction to Hydrogen Peroxide. *J. Am. Chem. Soc.* **2022**, *144*, 14505−14516.
(13) Shi, Y.; Li, M.; Yu, Y.; Zhang, B. Recent Advances in Nanostructured Transition Metal Phosphides: Synthesis and Energy-Related Applications. *Energy Environ. Sci.* **2020**, *13*, 4564−4582.
(14) Yang, B.; Xu, J.; Bin, D.; Wang, J.; Zhao, J.; Liu, Y.; Li, B.; Fang, X.; Liu, Y.; Qiao, L.; Liu, L.; Liu, B. Amorphous Phosphatized Ruthenium-Iron Bimetallic Nanoclusters with Pt-Like Activity for Hydrogen Evolution Reaction. *Appl. Catal. B Environ. Energy* **2021**, *283*, No. 119583.
(15) Li, B.-Q.; Zhang, S.-Y.; Chen, X.; Chen, C.-Y.; Xia, Z.-J.; Zhang, Q. One-Pot Synthesis of Framework Porphyrin Materials and Their Applications in Bifunctional Oxygen Electrocatalysis. *Adv. Funct. Mater.* **2019**, *29*, 1901301.
(16) Ding, K.; Hu, J.; Luo, J.; Zhao, L.; Jin, W.; Liu, Y.; Wu, Z.; Zou, G.; Hou, H.; Ji, X. Robust Electronic Correlation of Co-$CoN_4$ Hybrid Active Sites for Durable Rechargeable Zn-Air Batteries. *Adv. Funct. Mater.* **2022**, *32*, 2207331.
(17) Wang, M.; Ji, S.; Wang, H.; Wang, X.; Linkov, V.; Wang, R. Foamed Carbon-Supported Nickel-Iron Oxides Interspersed with Bamboo-Like Carbon Nanotubes for High-Performance Rechargeable Zinc-Air Batteries. *Small* **2022**, *18*, 2204474.
(18) Gao, Y.; Zheng, D.; Li, Q.; Xiao, W.; Ma, T.; Fu, Y.; Wu, Z.; Wang, L. 3D $Co_3O_4$-$RuO_2$ Hollow Spheres with Abundant Interfaces As Advanced Trifunctional Electrocatalyst for Water-Splitting and Flexible Zn−Air Battery. *Adv. Funct. Mater.* **2022**, *32*, 2203206.
(19) Zhang, B.; Shan, J.; Wang, W.; Tsiakaras, P.; Li, Y. Oxygen Vacancy and Core−Shell Heterojunction Engineering of Anemone-Like CoP@CoOOH Bifunctional Electrocatalyst for Efficient Overall Water Splitting. *Small* **2022**, *18*, 2106012.
(20) Zhang, J.; Wang, M.; Wan, T.; Shi, H.; Lv, A.; Xiao, W.; Jiao, S. Novel ($Pt$-$O_x$)-($Co$-$O_y$) Nonbonding Active Structures on Defective Carbon from Oxygen-Rich Coal Tar Pitch for Efficient HER and ORR. *Adv. Mater.* **2022**, *34*, 2206960.
(21) Meena, A.; Thangavel, P.; Jeong, D. S.; Singh, A. N.; Jana, A.; Im, H.; Nguyen, D. A.; Kim, K. S. Crystalline-Amorphous Interface of Mesoporous $Ni_2P$@$FePO_xH_y$ for Oxygen Evolution at High Current Density in Alkaline-Anion-Exchange-Membrane Water-Electrolyzer. *Appl. Catal. B Environ. Energy* **2022**, *306*, No. 121127.
(22) Zhang, P.; Wang, Y.; You, Y.; Yuan, J.; Zhou, Z.; Sun, S. Generation Pathway of Hydroxyl Radical in Fe/N/C-Based Oxygen Reduction Electrocatalysts under Acidic Media. *J. Phys. Chem. Lett.* **2021**, *12*, 7797−7803.
(23) Zhang, L.; Zhu, Y.; Nie, Z.; Li, Z.; Ye, Y.; Li, L.; Hong, J.; Bi, Z.; Zhou, Y.; Hu, G. Co/MoC Nanoparticles Embedded in Carbon Nanoboxes As Robust Trifunctional Electrocatalysts for a Zn−Air Battery and Water Electrocatalysis. *ACS Nano* **2021**, *15*, 13399−13414.
(24) Song, H.; Wu, M.; Tang, Z.; Tse, J. S.; Yang, B.; Lu, S. Single Atom Ruthenium-Doped CoP/CDs Nanosheets via Splicing of Carbon-Dots for Robust Hydrogen Production. *Angew. Chem., Int. Ed.* **2021**, *60*, 7234−7244.
(25) Guo, M.; Xu, M.; Qu, Y.; Hu, C.; Yan, P.; Isimjan, T. T.; Yang, X. Electronic/Mass Transport Increased Hollow Porous $Cu_3P$/MoP Nanospheres with Strong Electronic Interaction for Promoting Oxygen Reduction in Zn-Air Batteries. *Appl. Catal. B Environ. Energy* **2021**, *297*, No. 120415.
(26) Xu, F.; Cai, S.; Lin, B.; Yang, L.; Le, H.; Mu, S. Geometric Engineering of Porous PtCu Nanotubes with Ultrahigh Methanol Oxidation and Oxygen Reduction Capability. *Small* **2022**, *18*, 2107387.
(27) Zhao, Z.; Duan, L.; Zhao, Y.; Wang, L.; Zhang, J.; Bu, F.; Sun, Z.; Zhang, T.; Liu, M.; Chen, H.; Yang, Y.; Lan, K.; Lv, Z.; Zu, L.; Zhang, P.; Che, R.; Tang, Y.; Chao, D.; Li, W.; Zhao, D. Constructing Unique Mesoporous Carbon Superstructures via Monomicelle Interface Confined Assembly. *J. Am. Chem. Soc.* **2022**, *144*, 11767−11777.
(28) Yoo, J. M.; Shin, H.; Chung, D. Y.; Sung, Y.-E. Carbon Shell on Active Nanocatalyst for Stable Electrocatalysis. *Acc. Chem. Res.* **2022**, *55*, 1278−1289.
(29) Ding, K.; Hu, J.; Luo, J.; Jin, W.; Zhao, L.; Zheng, L.; Yan, W.; Weng, B.; Hou, H.; Ji, X. Confined N-$CoSe_2$ Active Sites Boost Bifunctional Oxygen Electrocatalysis for Rechargeable Zn−Air Batteries. *Nano Energy* **2022**, *91*, No. 106675.
(30) Liang, S.; Zou, L.-C.; Zheng, L.-J.; Li, F.; Wang, X.-X.; Song, L.-N.; Xu, J.-J. Highly Stable Co Single Atom Confined in Hierarchical Carbon Molecular Sieve As Efficient Electrocatalysts in Metal−Air Batteries. *Adv. Energy Mater.* **2022**, *12*, 2103097.
(31) Wang, Q.; Feng, Q.; Lei, Y.; Tang, S.; Xu, L.; Xiong, Y.; Fang, G.; Wang, Y.; Yang, P.; Liu, J.; Liu, W.; Xiong, X. Quasi-Solid-State Zn-Air Batteries With an Atomically Dispersed Cobalt Electrocatalyst and Organohydrogel Electrolyte. *Nat. Commun.* **2022**, *13*, 3689.
(32) Zhang, J.-Y.; Xia, C.; Su, Y.; Zu, L.; Zhao, Z.; Li, P.; Lv, Z.; Wang, J.; Mei, B.; Lan, K.; Zhao, T.; Zhang, P.; Chen, W.; Zaman, S.; Liu, Y.; Peng, L.; Xia, B. Y.; Elzatahry, A.; Li, W.; Zhao, D. Boosted Oxygen Kinetics of Hierarchically Mesoporous $Mo_2C$/C for High-current-density Zn−Air Battery. *Small* **2023**, *20*, 2307378.
(33) Shen, J.; Li, J.; Li, B.; Zheng, Y.; Bao, X.; Guo, J.; Guo, Y.; Lai, C.; Lei, W.; Wang, S.; Shao, H. Ambient Fast Synthesis of Superaerophobic/Superhydrophilic Electrode for Superior Electrocatalytic Water Oxidation. *Energy Environ. Sci.* **2022**, *6*, No. e12462.
(34) Xu, X.; Xie, J.; Liu, B.; Wang, R.; Liu, M.; Zhang, J.; Liu, J.; Cai, Z.; Zou, J. PBA-Derived FeCo Alloy with Core-Shell Structure Embedded in 2D N-Doped Ultrathin Carbon Sheets As a Bifunctional


https://doi.org/10.1021/acsnano.4c04479
*ACS Nano* 2024, 18, 17901−17912

Catalyst for Rechargeable Zn-Air Batteries. *Appl. Catal. B Environ. Energy* **2022**, *316*, No. 121687.
(35) Hou, C.-C.; Zou, L.; Sun, L.; Zhang, K.; Liu, Z.; Li, Y.; Li, C.; Zou, R.; Yu, J.; Xu, Q. Single-Atom Iron Catalysts on Overhang-Eave Carbon Cages for High-Performance Oxygen Reduction Reaction. *Angew. Chem., Int. Ed.* **2020**, *59*, 7384−7389.
(36) Kim, K.; Min, K.; Go, Y.; Lee, Y.; Shim, S. E.; Lim, D.; Baeck, S.-H. FeCo Alloy Nanoparticles Embedded in N-Doped Carbon Supported on Highly Defective Ketjenblack As Effective Bifunctional Electrocatalysts for Rechargeable Zn−Air Batteries. *Appl. Catal. B Environ. Energy* **2022**, *315*, No. 121501.
(37) Tong, M.; Yu, P.; Xie, Y.; Wang, L.; Wang, Y.; Fu, H. Atomically Dispersed Fe−$N_3C$ Sites Induce Asymmetric Electron Structures to Afford Superior Oxygen Reduction Activity. *Small* **2022**, *18*, 2201255.
(38) Lu, X.; Xu, H.; Yang, P.; Xiao, L.; Li, Y.; Ma, J.; Li, R.; Liu, L.; Liu, A.; Kondratiev, V.; Levin, O.; Zhang, J.; An, M. Zinc-Assisted MgO Template Synthesis of Porous Carbon-Supported Fe-$N_x$ Sites for Efficient Oxygen Reduction Reaction Catalysis in Zn-Air Batteries. *Appl. Catal. B Environ. Energy* **2022**, *313*, No. 121454.
(39) Xu, F.; Wang, J.; Zhang, Y.; Wang, W.; Guan, T.; Wang, N.; Li, K. Structure-Engineered Bifunctional Oxygen Electrocatalysts with $Ni_3S_2$ Quantum Dot Embedded S/N-Doped Carbon Nanosheets for Rechargeable Zn-Air Batteries. *Chem. Eng. J.* **2022**, *432*, No. 134256.
(40) Zhang, X.; Yan, J.; Lee, L. Y. S. Highly Promoted Hydrogen Production Enabled by Interfacial PN Chemical Bonds in Copper Phosphosulfide Z-Scheme Composite. *Appl. Catal. B Environ. Energy* **2021**, *283*, No. 119624.
(41) Wang, L.; Zhao, Y.; Huang, Z.; Rao, X.; Guo, M.; Isimjan, T. T.; Yang, X. Interfacial Regulation of Electron Enhanced $Co_2P$-$CuP_2$ Sheet-Like Heterostructure As a Robust Bifunctional Electrocatalyst for Overall Water Splitting and Zn-$H_2O$ Cell. *ChemCatChem.* **2022**, *14*, No. e202101933.
(42) Zhang, X.; Kim, D.; Guo, X.; Zhu, Y.; Lee, L. Y. S. Impacts of Boron Doping on the Atomic Structure, Stability, and Photocatalytic Activity of $Cu_3P$ Nanocrystals. *Appl. Catal. B Environ. Energy* **2021**, *298*, No. 120515.
(43) Liu, Q.; Liu, Q.; Kong, X. Cu-Based Nanosheet Arrays for Water-Splitting. *ACS Appl. Nano Mater.* **2019**, *2*, 6000−6009.
(44) Deng, D.; Qian, J.; Liu, X.; Li, H.; Su, D.; Li, H.; Li, H.; Xu, L. Non-Covalent Interaction of Atomically Dispersed Cu and Zn Pair Sites for Efficient Oxygen Reduction Reaction. *Adv. Funct. Mater.* **2022**, *32*, 2203471.
(45) Wang, H.; Wang, Y.; Zhang, J.; Liu, X.; Tao, S. Electronic Structure Engineering Through Fe-Doping CoP Enables Hydrogen Evolution Coupled with Electro-Fenton. *Nano Energy* **2021**, *84*, No. 105943.
(46) Chen, Y.; Yao, H.; Kong, F.; Tian, H.; Meng, G.; Wang, S.; Mao, X.; Cui, X.; Hou, X.; Shi, J. $V_2C$ MXene Synergistically Coupling FeNi LDH Nanosheets for Boosting Oxygen Evolution Reaction. *Appl. Catal. B Environ. Energy* **2021**, *297*, No. 120474.
(47) Yun, Y.; Xi, B.; Tian, F.; Chen, W.; Sun, W.; Pan, H.; Feng, J.; Qian, Y.; Xiong, S. Zero-Strain Structure for Efficient Potassium Storage Nitrogen-Enriched Carbon Dual-Confinement CoP Composite. *Adv. Energy Mater.* **2022**, *12*, 2103341.
(48) Chang, B.; Zhang, X.-G.; Min, Z.; Lu, W.; Li, Z.; Qiu, J.; Wang, H.; Fan, J.; Wang, J. Efficient Electrocatalytic Conversion of $CO_2$ to Syngas for the Fischer−Tropsch Process Using a Partially Reduced $Cu_3P$ Nanowire. *J. Mater. Chem. A* **2021**, *9*, 17876−17884.
(49) Liu, M.; Lu, B.-A.; Yang, G.; Yuan, P.; Xia, H.; Wang, Y.; Guo, K.; Zhao, S.; Liu, J.; Yu, Y.; Yan, W.; Dong, C.-L.; Zhang, J.-N.; Mu, S. Concave Pt−Zn Nanocubes with High-Index Faceted Pt Skin As Highly Efficient Oxygen Reduction Catalyst. *Adv. Sci.* **2022**, *9*, 2200147.
(50) Ding, K.; Hu, J.; Jin, W.; Zhao, L.; Liu, Y.; Wu, Z.; Weng, B.; Hou, H.; Ji, X. Dianion Induced Electron Delocalization of Trifunctional Electrocatalysts for Rechargeable Zn−Air Batteries and Self-Powered Water Splitting. *Adv. Funct. Mater.* **2022**, *32*, 2201944.
(51) Wang, X.; Zhao, L.; Li, X.; Liu, Y.; Wang, Y.; Yao, Q.; Xie, J.; Xue, Q.; Yan, Z.; Yuan, X.; Xing, W. Atomic-Precision $Pt_6$ Nanoclusters for Enhanced Hydrogen Electro-Oxidation. *Nat. Commun.* **2022**, *13*, 1596.
(52) Liu, M.; Wang, L.; Zhang, L.; Zhao, Y.; Chen, K.; Li, Y.; Yang, X.; Zhao, L.; Sun, S.; Zhang, J. In-Situ Silica Xerogel Assisted Facile Synthesis of Fe-N-C Catalysts with Dense Fe-$N_x$ Active Sites for Efficient Oxygen Reduction. *Small* **2022**, *18*, 2104934.
(53) Yang, Q.; Jia, Y.; Wei, F.; Zhuang, L.; Yang, D.; Liu, J.; Wang, X.; Lin, S.; Yuan, P.; Yao, X. Understanding the Activity of Co-$N_{4-x}C_x$ in Atomic Metal Catalysts for Oxygen Reduction Catalysis. *Angew. Chem., Int. Ed.* **2020**, *59*, 6122−6127.
(54) Yang, X.; Zheng, X.; Li, H.; Luo, B.; He, Y.; Yao, Y.; Zhou, H.; Yan, Z.; Kuang, Y.; Huang, Z. Non-Noble-Metal Catalyst and Zn/Graphene Film for Low-Cost and Ultra-Long-Durability Solid-State Zn-Air Batteries in Harsh Electrolytes. *Adv. Funct. Mater.* **2022**, *32*, 2200397.
(55) Liang, Z.; Kong, N.; Yang, C.; Zhang, W.; Zheng, H.; Lin, H.; Cao, R. Highly Curved Nanostructure-Coated Co, N-Doped Carbon Materials for Oxygen Electrocatalysis. *Angew. Chem., Int. Ed.* **2021**, *60*, 12759−12764.
(56) Tang, X.; Wei, Y.; Zhai, W.; Wu, Y.; Hu, T.; Yuan, K.; Chen, Y. Carbon Nanocage with Maximum Utilization of Atomically Dispersed Iron As Efficient Oxygen Electroreduction Nanoreactor. *Adv. Mater.* **2022**, *35*, 2208942.
(57) Sharma, M.; Jang, J.-H.; Shin, D. Y.; Kwon, J. A.; Lim, D.-H.; Choi, D.; Sung, H.; Jang, J.; Lee, S.-Y.; Lee, K. Y.; Park, H.-Y.; Jung, N.; Yoo, S. J. Work Function-Tailored Graphene via Transition Metal Encapsulation As a Highly Active and Durable Catalyst for the Oxygen Reduction Reaction. *Energy Environ. Sci.* **2019**, *12*, 2200−2211.
(58) Zhu, X.; Tan, X.; Wu, K.-H.; Haw, S.-C.; Pao, C.-W.; Su, B.-J.; Jiang, J.; Smith, S. C.; Chen, J.-M.; Amal, R.; Lu, X. Intrinsic ORR Activity Enhancement of Pt Atomic Sites by Engineering the d-Band Center via Local Coordination Tuning. *Angew. Chem., Int. Ed.* **2021**, *60*, 21911−21917.
(59) Wang, L.; Hao, Y.; Deng, L.; Hu, F.; Zhao, S.; Li, L.; Peng, S. Rapid Complete Reconfiguration Induced Actual Active Species for Industrial Hydrogen Evolution Reaction. *Nat. Commun.* **2022**, *13*, 5785.
(60) Hao, Y.; Yu, D.; Zhu, S.; Kuo, C.-H.; Chang, Y.-M.; Wang, L.; Chen, H.-Y.; Shao, M.; Peng, S. Methanol Upgrading Coupled with Hydrogen Product at Large Current Density Promoted by Atrong Interfacial Interactions. *Energy Environ. Sci.* **2023**, *16*, 1100−1110.
(61) Zhang, S.; Tan, C.; Yan, R.; Zou, X.; Hu, F.-L.; Mi, Y.; Yan, C.; Zhao, S. Constructing Built-In Electric Field in Heterogeneous Nanowire Arrays for Efficient Overall Water Electrolysis. *Angew. Chem., Int. Ed.* **2023**, *62*, No. e202302795.
(62) Wang, X.; Zhou, X.; Li, C.; Yao, H.; Zhang, C.; Zhou, J.; Xu, R.; Chu, L.; Wang, H.; Gu, M.; Jiang, H.; Huang, M. Asymmetric Co-$N_3P_1$ Trifunctional Catalyst with Tailored Electronic Structures Enabling Boosted Activities and Corrosion Resistance in an Uninterrupted Seawater Splitting System. *Adv. Mater.* **2022**, *34*, 2204021.
(63) Li, Y.; Lu, X. F.; Xi, S.; Luan, D.; Wang, X.; Lou, X. W. Synthesis of N-Doped Highly Graphitic Carbon Urchin-Like Hollow Structures Loaded with Single-Ni Atoms towards Efficient $CO_2$ Electroreduction. *Angew. Chem., Int. Ed.* **2022**, *61*, No. e202201491.
(64) Kreider, M. E.; Gunasooriya, G. T. K. K.; Liu, Y.; Zamora Zeledón, J. A.; Valle, E.; Zhou, C.; Montoya, J. H.; Gallo, A.; Sinclair, R.; Nørskov, J. K.; Stevens, M. B.; Jaramillo, T. F. Strategies for Modulating the Catalytic Activity and Selectivity of Manganese Antimonates for the Oxygen Reduction Reaction. *ACS Catal.* **2022**, *12*, 10826−10840.
(65) Huang, Y.; Fang, Y.; Lu, X. F.; Luan, D.; Lou, X. W. $Co_3O_4$ Hollow Nanoparticles Embedded in Mesoporous Walls of Carbon Nanoboxes for Efficient Lithium Storage. *Angew. Chem., Int. Ed.* **2020**, *59*, 19914−19918.


https://doi.org/10.1021/acsnano.4c04479
*ACS Nano* 2024, 18, 17901−17912

(66) Kong, F.; Cui, X.; Huang, Y.; Yao, H.; Chen, Y.; Tian, H.; Meng, G.; Chen, C.; Chang, Z.; Shi, J. N-Doped Carbon Electrocatalyst: Marked ORR Activity in Acidic Media without the Contribution from Metal Sites. *Angew. Chem., Int. Ed.* **2022**, *61*, No. e202116290.
(67) Qiu, L.; Wang, Q.; Yan, P.; Yu, X.-Y. Chemical-Physical Synergistic Etching Enabling Deep Reconstruction of NiFe Prussian Blue Analogue for Efficient Oxygen Evolution Reaction and Zn-Air Batteries. *J. Mater. Chem. A* **2022**, *10*, 21251−21259.



https://doi.org/10.1021/acsnano.4c04479
*ACS Nano* 2024, 18, 17901−17912